aerospace

MDPI

Article

Fast-Responding Pressure-Sensitive Paint Measurements of the IC3X at Mach 7.2

Valeria Delgado Elizondo, Abinayaa Dhanagopal and Christopher S. Combs *

Department of Mechanical Engineering, Margie and Bill Klesse College of Engineering and Integrated Design, The University of Texas at San Antonio, San Antonio, TX 78249, USA; abinayaa.dhanagopal@my.utsa.edu (A.D.)
* Correspondence: christopher.combs@utsa.edu; Tel.: +1-(210)-458-8288

Abstract: Global surface pressure measurements of a 5.7% scale AFRL Initial Concept 3.X vehicle (IC3X) were obtained using a fast-responding ruthenium-based pressure-sensitive paint (PSP) at the UTSA Mach 7 Ludwieg Tube Wind Tunnel at two different angles of attack, 0° and 2.5°. Static calibration of the paint was performed over a range of 0.386 kPa to 82.7 kPa to relate luminescent intensity to pressure. Details on the facility, paint preparation, application, calibration, and image processing techniques are provided in the manuscript. The results from statistical, spectral, and proper orthogonal decomposition (POD) analyses are presented to characterize the pressure field observed on the model. The experimental results qualitatively follow the expected trends and correspond to the occurrence of shock waves and expansion fans, which were visualized via Schlieren imaging. The theoretical pressure range obtained from conical shock analysis for 0° agrees with the experimentally derived pressure range for the model, and the outliers are attributed to errors in image registration. This study presents preliminary pressure measurements that pave the way for obtaining time-resolved global PSP measurements to train and validate aerothermodynamic machine learning models.

Keywords: pressure-sensitive paint; Ludwieg tube; wind tunnel; hypersonics

Citation: Delgado Elizondo, V.; Dhanagopal, A.; Combs, C.S. Fast-Responding Pressure-Sensitive Paint Measurements of the IC3X at Mach 7.2. *Aerospace* **2023**, *10*, 890. https://doi.org/10.3390/aerospace10100890

Academic Editor: Sebastian Karl

Received: 23 September 2023
Revised: 13 October 2023
Accepted: 15 October 2023
Published: 18 October 2023

1. Introduction

Hypersonic aircraft development is impeded by the technical challenges arising from extreme temperatures and pressures experienced when cruising at high speeds [1,2]. While experimental campaigns can provide valuable information to help tackle this, the prohibitive costs associated with flight testing have significantly limited their use in hypersonic aircraft development [3]. Therefore, researchers have attempted to maximize the amount of data collected during these rare experimental campaigns. In order to increase the amount of usable information gained from real-life test flights, machine learning (ML) algorithms incorporated with anchoring-measured values obtained from sparsely distributed sensors have been proposed to predict the remainder of the values that are not directly measured. These models can only be validated and optimized by using experimental data encompassing the interaction effects along the entire surface of the vehicle. Pressure taps are used in experiments to measure surface pressure in aerodynamic models [4,5], but these measurements are intrusive and limited by the spatial resolution that can be achieved due to the physical size of the pressure transducers.

Non-intrusive techniques such as pressure-sensitive paint (PSP) and temperature-sensitive paint (TSP) are ideal candidates for obtaining global surface measurements that can then be provided to train and validate ML models geared toward hypersonic applications. While the development of ML models is outside of the scope of this present study, the objective here was to demonstrate a robust and cost-effective means for generating training data for these models in hypersonic test facilities. An added advantage of PSP is that it can also be used in conjunction with other non-intrusive optical techniques like Schlieren, IR

thermography, and TSP [6]. Unlike traditional transducers and probes that offer discrete point measurements, PSP provides aerothermodynamic data across a three-dimensional surface, making it valuable for hypersonic flows. Although slow response times were a limiting factor in the past, the advent of fast PSP formulations and recent advancements in PSP measurement technology have made it possible to accurately measure global surface pressure distributions and fluctuations across transonic, supersonic, and hypersonic regimes. Notable examples include the NASA Ames Unitary 11ft. Wind Tunnel experiment on the Space Launch System [7–10], hypersonic boundary layer separation studies conducted by Running et al. on a conical structure resembling HiFire-I at the University of Notre Dame's pulsed arc-heated hypersonic wind tunnel (ACT-1) [11], and the surface pressure measurements of an elliptic cone body at Mach 7.5 in the Calspan University of Buffalo Research Center's hypersonic shock tunnel [12].

One key advantage of using PSP is its suitability for application on surfaces of wind tunnel models with thin profiles and surface installation constraints, which would otherwise make the use of pressure transducers unfeasible [13,14]. This includes geometries such as rocket fins, turbomachinery blades, and wing tips [15,16]. While the initial setup costs and material costs for PSP may be slightly higher than those associated with pressure transducers, it is significantly more cost-effective in the long run as it requires little to no maintenance instrumentation for data acquisition and offers higher spatial resolution [17–19].

The history and operating principle of PSPs have been sufficiently documented in the literature [17,18] and are briefly discussed here. PSP is an optical sensor operating on the well-established mechanism of luminescence. Luminophore molecules embedded within an oxygen-permeable binder are excited when illuminated with an ultraviolet-light-emitting diode (LED). These molecules transition to an excited energy state and emit a fluorescent signal in the 600 nm range upon recovery to their ground state [19]. The fluorescent signal can be related to the static pressure of air with a reference intensity and a known reference pressure through the Stern–Volmer relationship [20]. The luminescent emission is affected by photophysical processes. In PSP, that process is oxygen-quenching, as discussed by Liu et al. [21]. The oxygen molecules interact with the embedded luminophore molecules through the oxygen-permeable binder layer. In accordance with Henry's law, the concentration of oxygen molecules in a PSP layer is proportional to the partial pressure of oxygen in the test gas above the surface coated with PSP. Pressure is proportional to the partial pressure of oxygen. At high pressures, the concentration of oxygen molecules in the PSP layer is higher, resulting in increased quenching. Therefore, as pressure increases, a decrease in luminescent intensity is observed. In fast PSP, the binder layer is porous, and the oxygen quenching process occurs in shorter timescales, which allows for the detection of rapid pressure fluctuations experienced by the model.

This study used a ruthenium-based fast PSP prepared in-house to obtain high-speed, spatially resolved global surface pressure distributions along the Initial Concept 3. X vehicle [22] (IC3X) encountering hypersonic flow for overall test durations of 300–500 ms at different angles of attack. The use of PSP, although prevalent in aerodynamic applications across subsonic [22,23] and supersonic flow regimes [24,25], has seen limited use in the hypersonic domain. Only a handful of researchers have leveraged this technique to investigate surface pressure trends on axisymmetric models in the hypersonic domain: Running and Juliano [26] applied anodized aluminum PSP to a cone flare model at Mach 6.25 to obtain global measurements of the hypersonic shockwave/boundary-layer interactions; Nakakita and Asai [27] applied fast PSP on a 3D winged geometry at Mach 10. The current study is among the first to use fast PSP on a finned axisymmetric geometry experiencing Mach 7.2 in an impulse facility.

2. Materials and Methods

2.1. Experimental Facility

The experimental campaign was conducted at the hypersonic Ludwieg Tube Wind Tunnel facility located at UTSA. This facility can generate a freestream Mach number of

7.2 ± 0.2 [28,29]. Figure 1 illustrates a CAD rendering of the UTSA Mach 7 wind tunnel, highlighting its main components. With a stagnation pressure and temperature of 13.79 MPa (2000 psi) and 700 K (1260 °R), respectively, the wind tunnel is capable of achieving unit Reynolds numbers of up to 200 × 10^6 m^{-1} (61.0 × 10^6 ft^{-1}) [28]. A comprehensive characterization of this facility can be found in the work of Hoffman et al. [23,28].

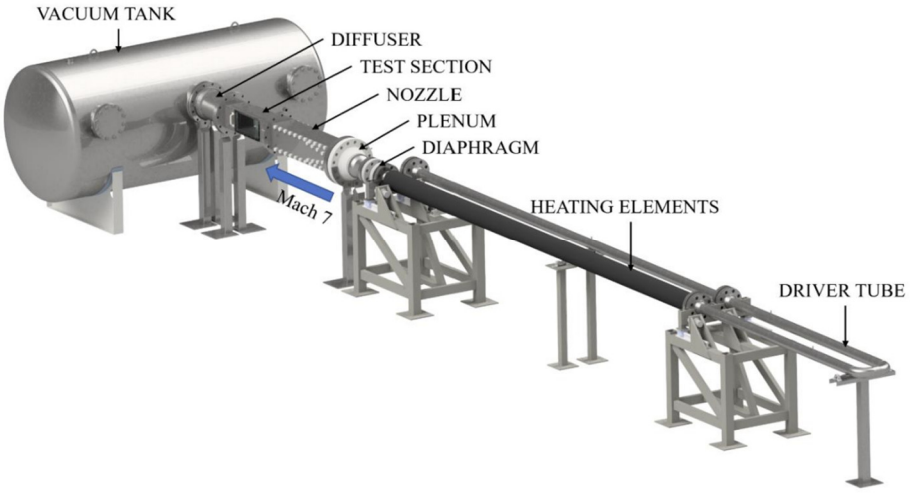

Figure 1. CAD rendering of the UTSA Mach 7 Ludwieg Tube Wind Tunnel.

Wind tunnel tests commence by rupturing a thin aluminum diaphragm that separates the 18.29 m (60 feet) long driver tube from the rest of the system. Prior to testing, the entire system is evacuated to a vacuum pressure of approximately 1.6 torr (0.03 psi) to remove moisture and prevent condensation during rapid expansion in the converging-diverging nozzle. The driver tube is then pressurized with dry compressed air at a steady rate of approximately 68.95 kPa/min. The test section features a constant cross-sectional area of 0.20 m × 0.20 m (8 in × 8 in) and is optically accessible through acrylic windows. Downstream of the test section, the hypersonic airflow passes through a diffuser to decelerate and is brought to rest in a 6.06 m^3 (1600 gallon) vacuum chamber. The duration of each test in this facility is approximately 450 ms, consisting of multiple steady-state passes lasting 50 to 100 ms each [28]. A more comprehensive description of the facility's design and capabilities can be found in the works of Bashor et al. [30] and Hoffman et al. [31].

2.2. Model Geometry

The Initial Concept 3.X vehicle (IC3X) studied here has been adopted by multiple teams across the FAST initiative to facilitate the comparison of experimental results. The geometry of this model was outlined in detail by Klock [32]. This geometry was manufactured in-house using a 3D printer on a 5.7% scale with an overall length of 20.3 cm to ensure complete visibility and to fit the test section. The material used was a photopolymer resin developed by Formlabs [33] and was chosen for its flexure strength. Undesired roughness on the model was eliminated by sanding prior to tests. The model was sting-mounted into the wind tunnel test section, with two different inserts manufactured to achieve the 0° and 2.5° AoAs. Further details of the dimensions and material properties can be found in Table 1. Figure 2 shows a rendering of the UTSA IC3X model.

2.3. PSP Preparation and Application

The fast PSP formulation employed in this study was a single-luminophore, porous, ruthenium-based polymer/ceramic PSP (PC-PSP) originally formulated by Egami et al. [34]. This formulation was chosen due to the high porosity of the polymer and the quick response time of the luminophore, making it an optimal choice for testing at the UTSA Mach 7 facility. The paint mixture consisted of tris(4,7-diphenyl-1,10-phenanthroline) ruthenium (II) dichloride (Ru(dpp)3) as the luminophore dye. The polymer used was ShinEtsu

Silicone adhesive glue (silicone) from Shin-Etsu Polymer Co., Ltd., Tokyo, Japan and the ceramic particles employed were titanium dioxide (TiO_2). The solvent mixture consisted of dichloromethane (DCM) with a purity of ≥99.8% (containing 40–150 ppm amylene as a stabilizer) and toluene with a purity of ≥99.8%. The solute composition comprised 92.4% TiO_2, 6.6% silicone, and 0.99% luminophore, while the paint solvent comprised 40% DCM and 60% toluene. The required amount of silicone for paint preparation was accurately weighed using a U.S. Solid digital balance scale. The solvent was prepared by adding toluene to the silicone after DCM, and the three ingredients were mixed using a magnetic stirrer for 20 min to ensure complete dissolution of the silicone. The TiO_2 and luminophore were weighed separately and added to the solvent. The resulting mixture was placed in a tightly sealed paint vial and immersed in a sonicator for 10 min to guarantee the homogeneity of the paint.

Table 1. UTSA IC3X model properties.

Property	Value
Body Length	20.3 cm
Body Diameter	2.05 cm
Wingspan	4.67 cm
Tensile Strength	65 MPa
Bending Modulus	2.2 GPa
Mass (g)	45

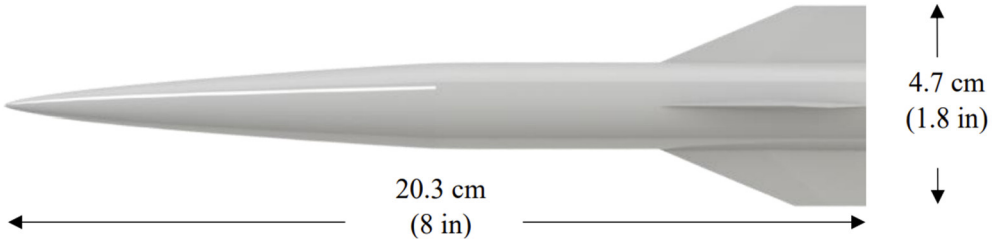

Figure 2. CAD rendering of the UTSA IC3X wind tunnel model.

For paint application, a high-pressure, low-volume (HPLV) spray gun was employed at a pressure of 140 kPa (20 psi), with the pressure regulator on the spray gun used to maintain a constant application pressure. Compressed air supplied by a McGraw compressor with a pressure of 758.4 kPa was used. The spray gun was held perpendicular to the target surface at an approximate distance of 20 cm (8 in), and the paint was applied at a steady rate and in alternating directions along a selected axis. The paint layer was allowed to dry between each pair of strokes for a few seconds to prevent smearing. The paint was applied in low-volume sets to minimize material waste that could result from rapid solvent evaporation. The paint was poured into the spray gun in 15 mL sets, and any solid residue was cleaned and unclogged between sets. It was previously observed that the thickness of the paint layer and the number of paint strokes do not follow a linear relationship due to spray gun operator error [35]. Therefore, the test surface was coated until the paint in the spray gun chamber was exhausted, and the surface was inspected to ensure complete coverage and a uniform thickness.

2.4. Experimental Setup

The IC3X model was mounted on a sting at the desired angle of attack (AoA) and coated with fast PSP. Subsequently, the painted model was mounted onto the wind tunnel test section. PSP images were captured using a high-speed camera(Fastcam SA-Z, Photron Ltd., Tokyo, Japan) which offers frame rates of up to 2.1 MHz and exposure times as short as 159 ns, making it suitable for Mach 7 flow applications. The high-speed camera was positioned perpendicular to the model.

A UV-light-emitting diode (LED) with peak irradiance at 405 nm (Luminous CBM-120-UV) was employed to excite the PSP. The LED was powered by a CUVEE Low-Voltage High-Current LED Driver, which enabled the pulsing of the LED for the duration of the camera shutter. The following optics were installed ahead of the camera:

1. A Schott RG-610 long-pass filter with a cut-on wavelength of 610 nm and stopband and passband limits of 503 nm and 690 nm, respectively, with block wavelengths outside the PSP emission band.
2. An anti-reflection (AR) filter was employed to minimize reflections. These filters ensured that the brightness in the captured images corresponded exclusively to the luminescence emitted by the PSP.
3. A Fresnel lens was installed to collimate the UV LED output.

The experimental setup is depicted below in Figure 3.

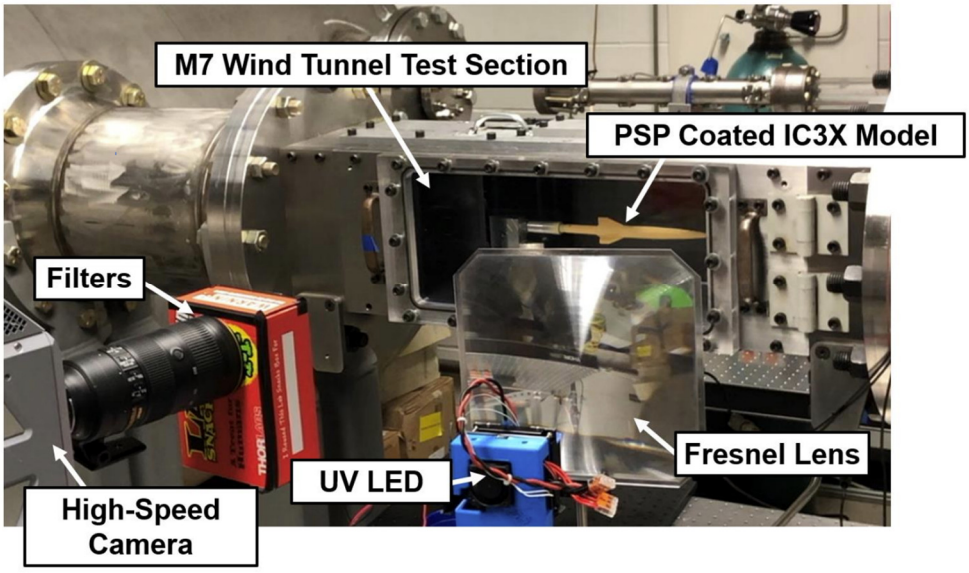

Figure 3. IC3X PSP wind tunnel experimental setup.

2.5. PSP Static Calibration Setup

Static calibration of the fast PSP was carried out by placing PSP-coated thin aluminum plates measuring 5.08 cm × 6.35 cm (2 in × 2.5 in) inside a 12.7 cm × 12.7 cm × 19.05 (5 in × 5 in × 7.5 in) rectangular aluminum vacuum chamber. Optical access was provided on one face of the chamber through a 0.64 cm (0.25 in) thick acrylic window. The desired vacuum level was achieved using a Sogevac 65B vacuum pump. The calibration setup included the positioning of a Photron Fastcam SA-Z high-speed camera perpendicular to the surface of the test plate, a UV LED with peak irradiance at 405 nm, and the utilization of optical filters and a Fresnel lens, as previously described. The static calibration experimental setup is illustrated in Figure 4.

2.6. Wind Tunnel Data Processing

Images of the PSP-coated IC3X model during wind tunnel tests were captured using a high-speed camera operating at a frame rate of 20 kHz. These images, referred to as "wind-on" images, were taken upon the rupture of the diaphragm, signifying the initiation of airflow downstream into the test section as the wind tunnel starts. The images corresponding to the first steady-state pass were selected by identifying the start time and duration of the pass using stagnation and static pressure data, along with the camera trigger signal acquired using a LabView program. For the 0° AoA case, the duration of the first pass was 63.6 ms, resulting in 1272 images, while for the 2.5° AoA case, the first pass lasted 58.8 ms, yielding 1176 images. The data processing flowchart shown in Figure 5 details the steps undertaken to convert intensities to pressure. Here, the 3 inputs and the output of the

code are indicated by red boxes and all other steps are included in black boxes. As the PSP used in this study was prepared in-house, multiple experiments on both the 0° and 2.5° AoA were conducted to better understand the paint response and its characteristics while also ensuring repeatability between tests. Across all 3 tests in the experimental campaign, the pressure distribution on the IC3X followed expected trends.

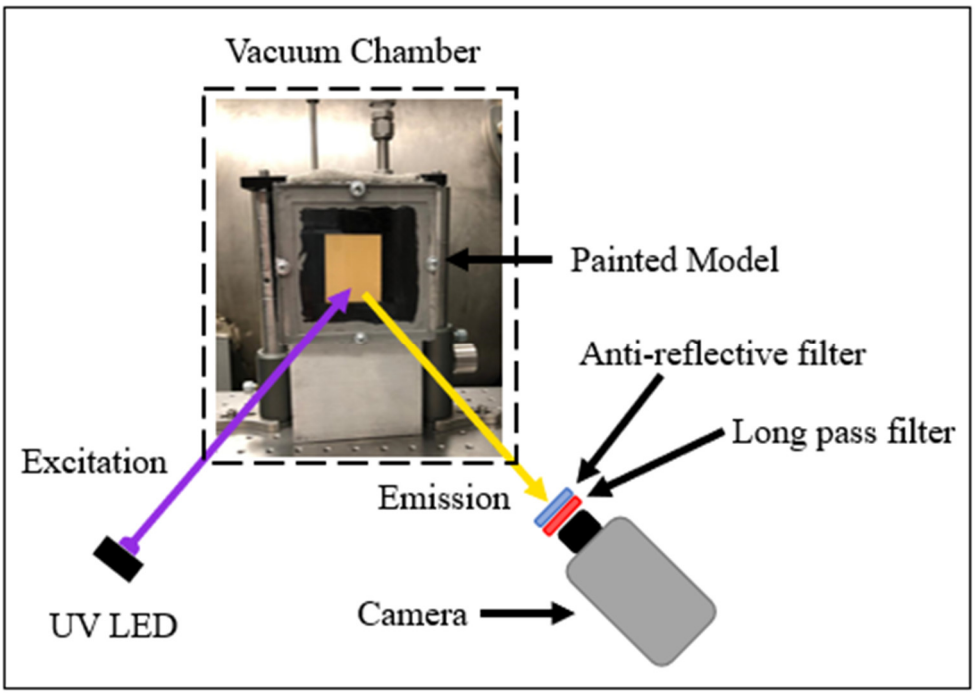

Figure 4. PSP static experimental setup block diagram.

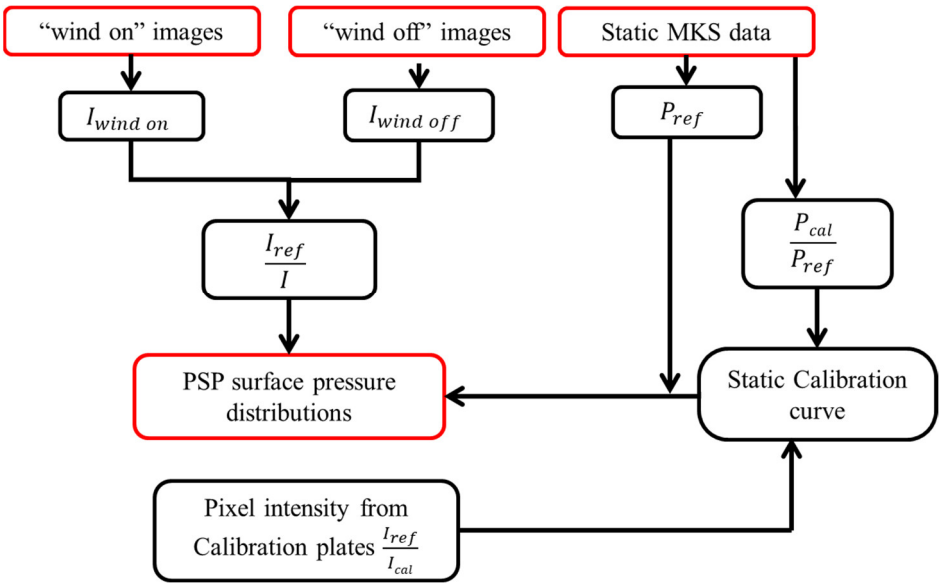

Figure 5. Data processing roadmap.

Reference images, or "wind-off" images, were taken at a low vacuum pressure once the whole system drawdown was completed. These reference images were also captured at a frame rate of 20 kHz, but the recording time was limited to less than a second to minimize paint degradation due to exposure to UV light. The original image resolution was 1024 × 1024 pixels; however, the images were further cropped to reduce the background area and decrease computation time. The reference image used for normalizing

the instantaneous images was an average of 200 images taken over a duration of 10 ms to mitigate noise.

The image registration algorithm developed by Guizar-Sicairos et al. [36] was employed to align the wind-off reference image with the wind-on instantaneous images, achieving sub-pixel accuracy. The division of these images resulted in reference intensity over instantaneous intensity ratios. Subsequently, the normalized images were shifted to the wind-off position using the affine transformation available in the OpenCV-Python library [37]. The transformation matrix used the initially determined shift between the wind-on and wind-off images to align them, producing normalized images in the same position. This realignment of the image set facilitated the tracking of pressure fluctuations at points of interest on the model's surface and enables statistical analysis. The resulting images were 2D matrices with entries corresponding to intensity ratios. The intensity ratio matrix was then converted into a pressure ratio matrix using the calibration curve equation specific to the wind tunnel test. Finally, the pressure ratio matrix was multiplied by the reference pressure, yielding a 2D global pressure field of the IC3X model.

3. Results and Discussion

3.1. Static Calibration Curve

Static calibration experiments were performed to establish the relationship between the PSP intensity and pressure. Images of a PSP-coated thin aluminum plate were acquired at a frame rate of 1000 fps while the pressure in the chamber was gradually reduced from 82.7 kPa (12 psi) to 0.386 kPa (0.06 psi) over 32.5 s. The acquired images were saved as an MRAW file, and the pymraw module developed by Javh et al. [38] was used to load the images directly from the MRAW file.

The experimental plates exhibited small-scale unevenness in paint concentration and illumination. A focus area within the plate was selected and averaged to mitigate the influence of these variations on establishing the relationship between pressure and paint emission intensity. This approach yielded a singular intensity value corresponding to a specific static pressure. The calibration measurements were then normalized using the reference pressure obtained from a wind tunnel test and the corresponding intensity of the PSP-coated plate at that pressure. The resulting normalized ratios generated a calibration curve specific to the particular wind tunnel run, relating intensity ratios to pressure ratios. It is worth noting that pressure-sensitive paint experiences luminescent decay due to its photosensitivity property [21]. In this study, multiple plates coated with pressure-sensitive paint (PSP) were imaged inside a vacuum chamber while the pressure was gradually reduced from 82.7 kPa (12 psi) to 0.386 kPa (0.06 psi) over 32.5 s at a frame rate of 1000 fps. Pressure and intensity measurements were normalized using the reference pressure obtained from the wind-off images of the IC3X model. Following normalization, pressure and intensity were related using a second-degree polynomial interpolation.

Figure 6 illustrates the average static calibration curve, showing a parabolic relationship between pressure and intensity values for all three calibration plates. Calibration constants A, B, and C were acquired; following this, the curve fit form for the PSP given in Equation (1) [21] was used to convert intensity ratios to pressure ratios.

$$\frac{I_{ref}}{I} = A + B \cdot \left(\frac{P}{P_{ref}}\right) + C \cdot \left(\frac{P}{P_{ref}}\right)^2 \quad (1)$$

The prepared paint was found to respond to pressure changes at Mach 7.2, and the coherence of the spectra, as shown in Figure 7, was calculated to compare the similarity of the signals at different frequencies. It was found that, on a canonical wall-to-wall flat-plate model, the paint exhibited a ~7 kHz response rate with a 68% coherence to Kulite transducers, as reported in [39].

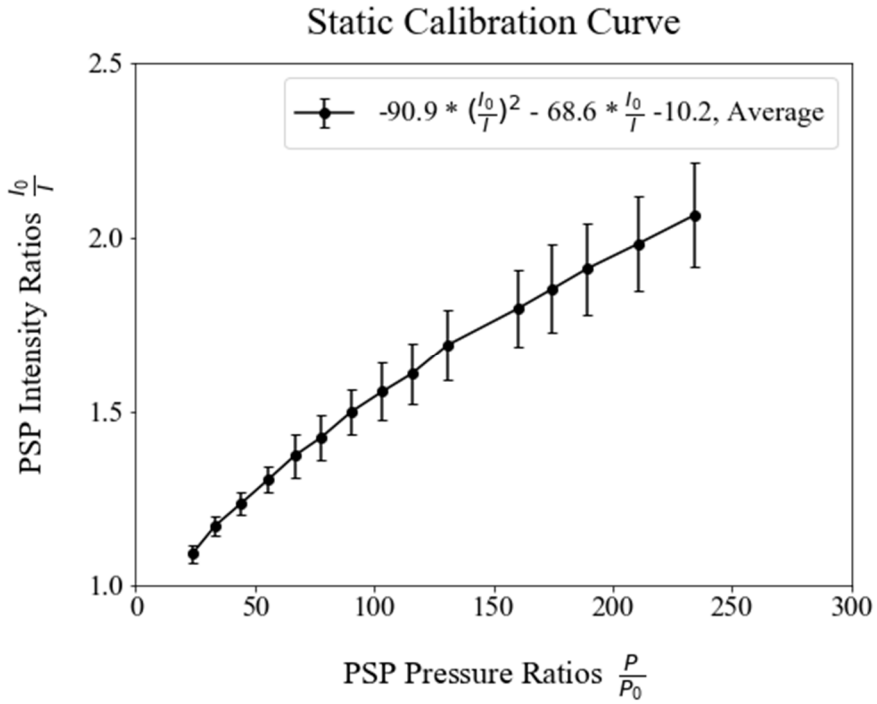

Figure 6. Experimental pressure-sensitive paint static calibration curves.

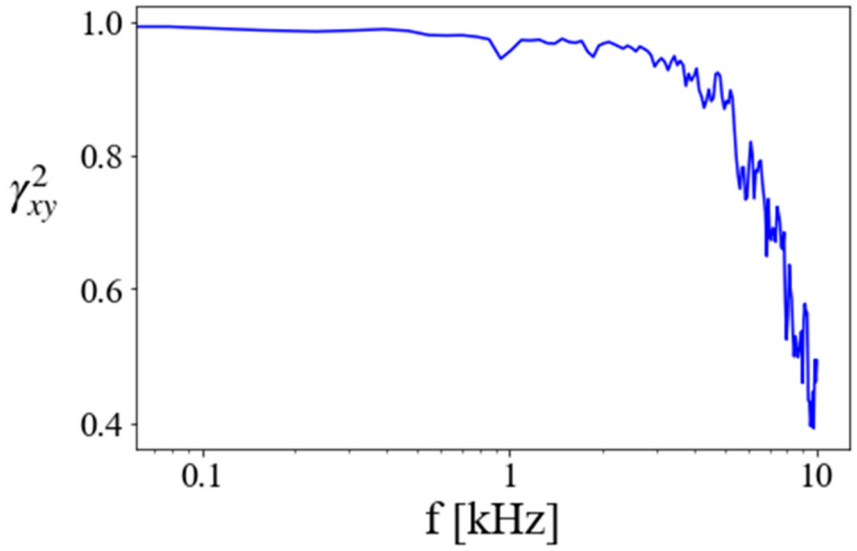

Figure 7. Coherence of paint response on a canonical flat plate model from [39].

3.2. Photodegradation

The rate of paint degradation was estimated during a constant-pressure interval for each calibration plate. Figure 8 illustrates the percentage loss in counts per second of exposure from the initial intensity recording. The figure shows a linear degradation trend, with an average degradation rate of 2.9% per second of UV LED exposure. For wind tunnel tests lasting less than 250 ms, such as the ones conducted in this study, the less than 1% loss in counts does not significantly affect the results. However, experiments with durations exceeding 1 s, such as calibration experiments, experience a more noticeable impact from the loss in counts. Therefore, the degradation trends identified were used as correction factors for static calibration calculations.

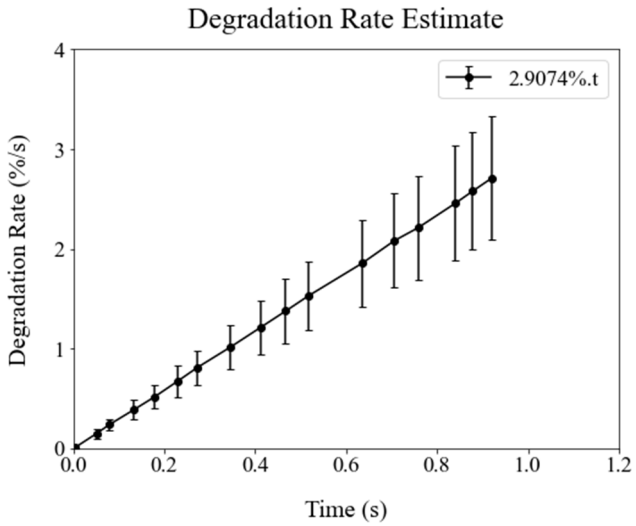

Figure 8. PSP degradation rate estimates.

Figure 9 presents the loss in counts as a function of time at relatively constant static pressure and the intensity readings after the correction factors were applied. The correction factors were applied to the calibration data sets prior to averaging to mitigate the effects of photodegradation.

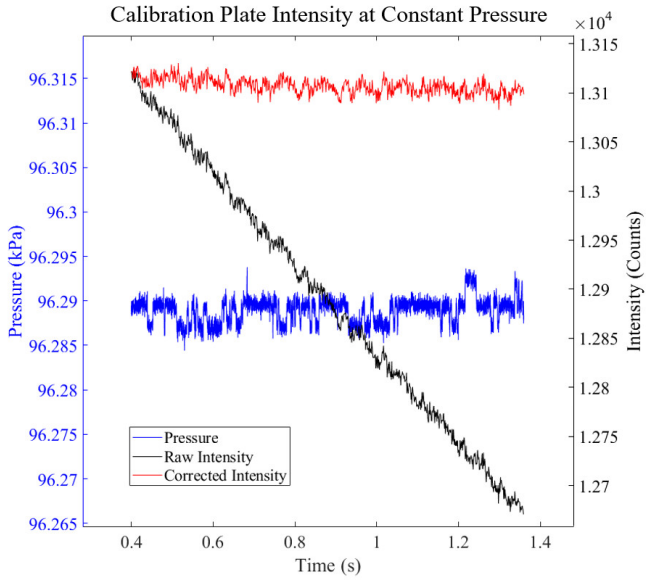

Figure 9. Raw and corrected intensity at constant pressure.

3.3. Schlieren

Schlieren experiments were conducted at a 0° AoA to visualize the flow structures surrounding the model. The results indicate the presence of a conical shock from the nose, an expansion fan from the ogive/cylinder geometry interface, and a subsequent compression and expansion fan along the fin geometry. These flow structures align with the expected pressure distribution derived from the average pressure maps obtained from PSP measurements.

The highest pressure is expected at the nose of the vehicle, directly behind the conical shock. This is because the surface of the nose is the first geometry that obstructs and compresses the incoming hypersonic flow. As the flow progresses along the ogive, the pressure gradually decreases. An expansion fan is formed downstream of the vehicle at the ogive/cylinder interface. At this point, the geometry ceases to obstruct the flow and

provides a constant surface through which the flow can travel, resulting in a significant pressure decrease. Moving further downstream to the fins, a similar behavior to the nose is observed, where the fins block the incoming flow and induce a higher pressure.

Figure 10 shows an overlay of the Schlieren and PSP results, providing a visual representation of the main flow structures identified in the experiment.

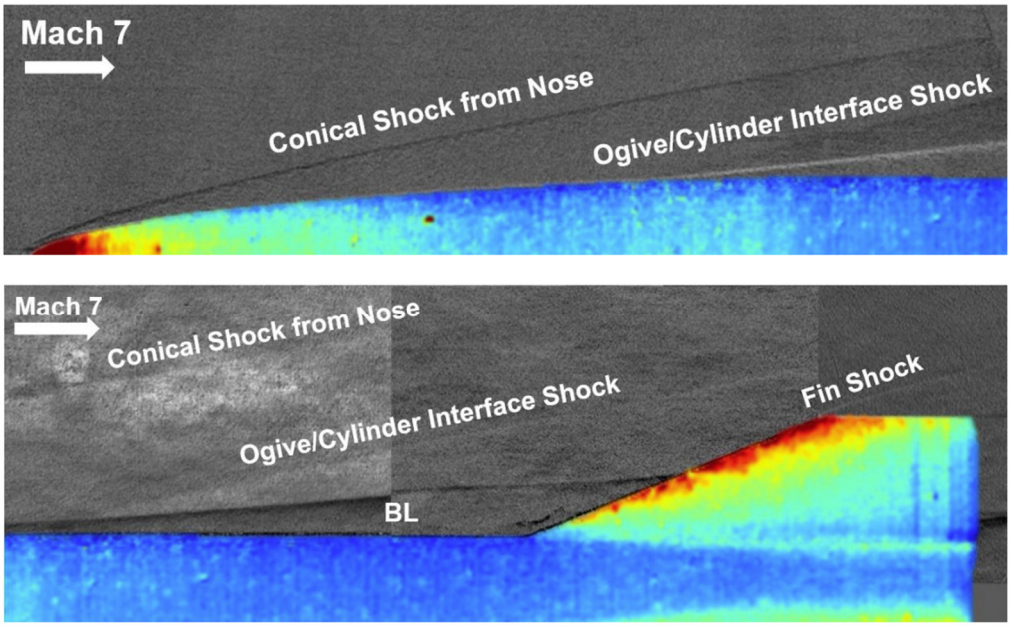

Figure 10. Overlay of Schlieren- and PSP-derived pressure field at 0° AoA.

3.4. Pressure Measurements—Statistical Analysis

Images of the pressure-sensitive paint (PSP) coated IC3X model were captured at 0° and 2.5° AoAs during a wind tunnel test under Mach 7. The first steady-state pass of the 0° AoA case comprised 1272 images, while the 2.5° AoA case encompassed 1176 images. These image sets were used to perform statistical and spectral analysis of the pressure field for both cases. Figure 11 illustrates the instantaneous pressure fields, and Figure 12 displays the average pressure fields.

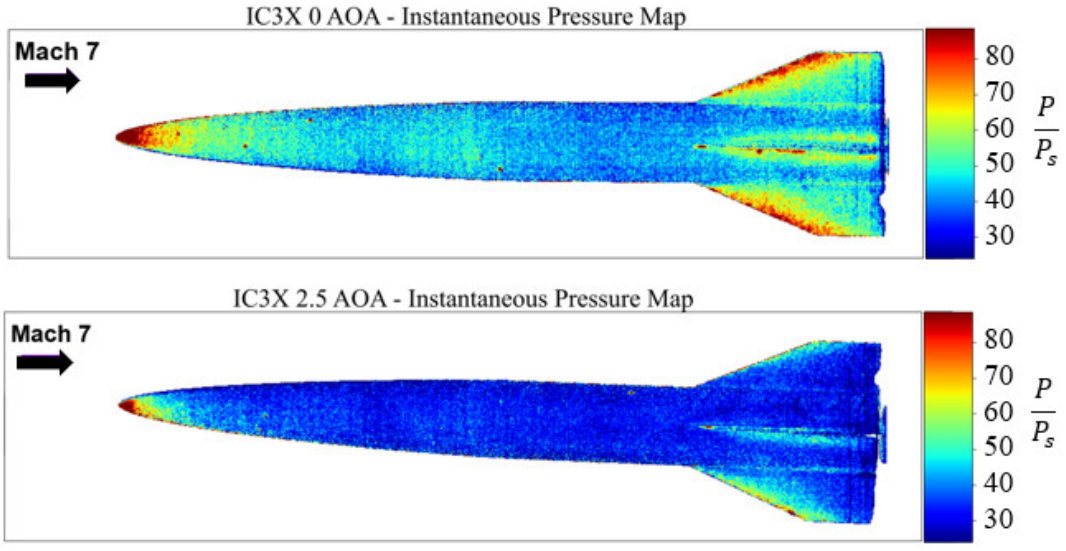

Figure 11. Instantaneous pressure fields.

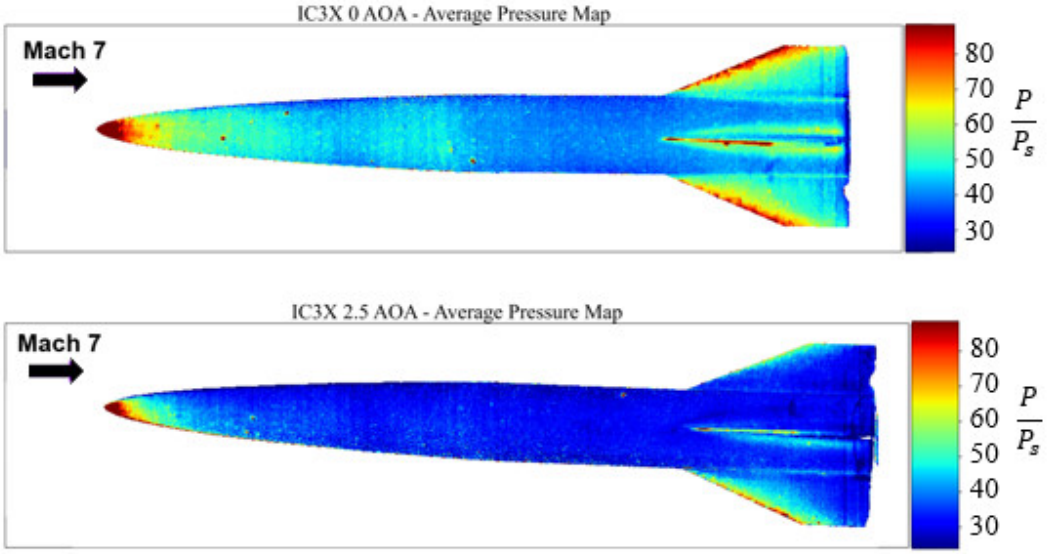

Figure 12. Average pressure fields.

The 2D maps of pressure distribution demonstrate smooth areas of higher or lower pressure, as expected, with the exception of a few speckle-like markings, where pressure appears to intensify upstream of the model. These markings correspond to paint solute aggregates that did not dissolve thoroughly in the solvent. The overall pressure distribution across a model qualitatively follows expected trends, as outlined in the Schlieren flow visualization presented in the previous section. Both models indicate high-pressure regions at the nose and fin, an initial pressure reduction downstream of the nose, and another significant pressure reduction following the ogive–cylinder interface where the expansion fan occurs. All pressure fields are normalized by the static pressure in the test section.

3.5. Power Spectral Density (PSD) Analysis

Pressure time histories and power spectral densities (PSDs) were retrieved from five areas of interest in the IC3X model: the nose, upstream, downstream, interaction region between a fin and the fuselage, and fin edge. The instantaneous measurements represent the average of a 49-square pixel area centered at each location of interest. These areas are indicated and labeled in Figure 13 for the 0° AoA case and Figure 14 for the 2.5° AoA case.

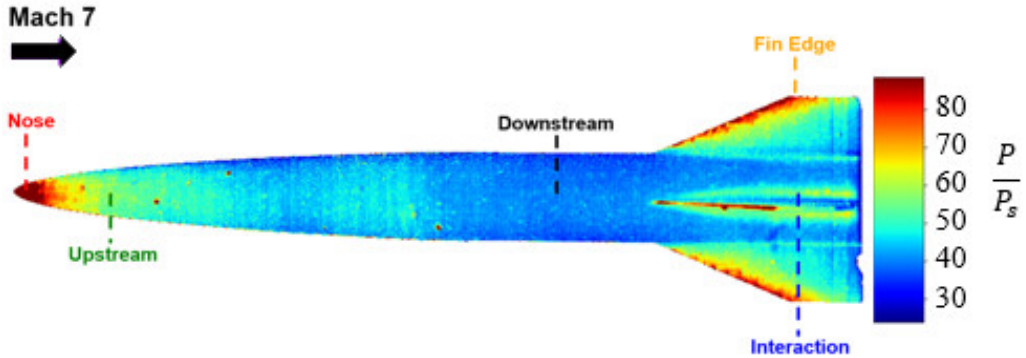

Figure 13. *Cont.*

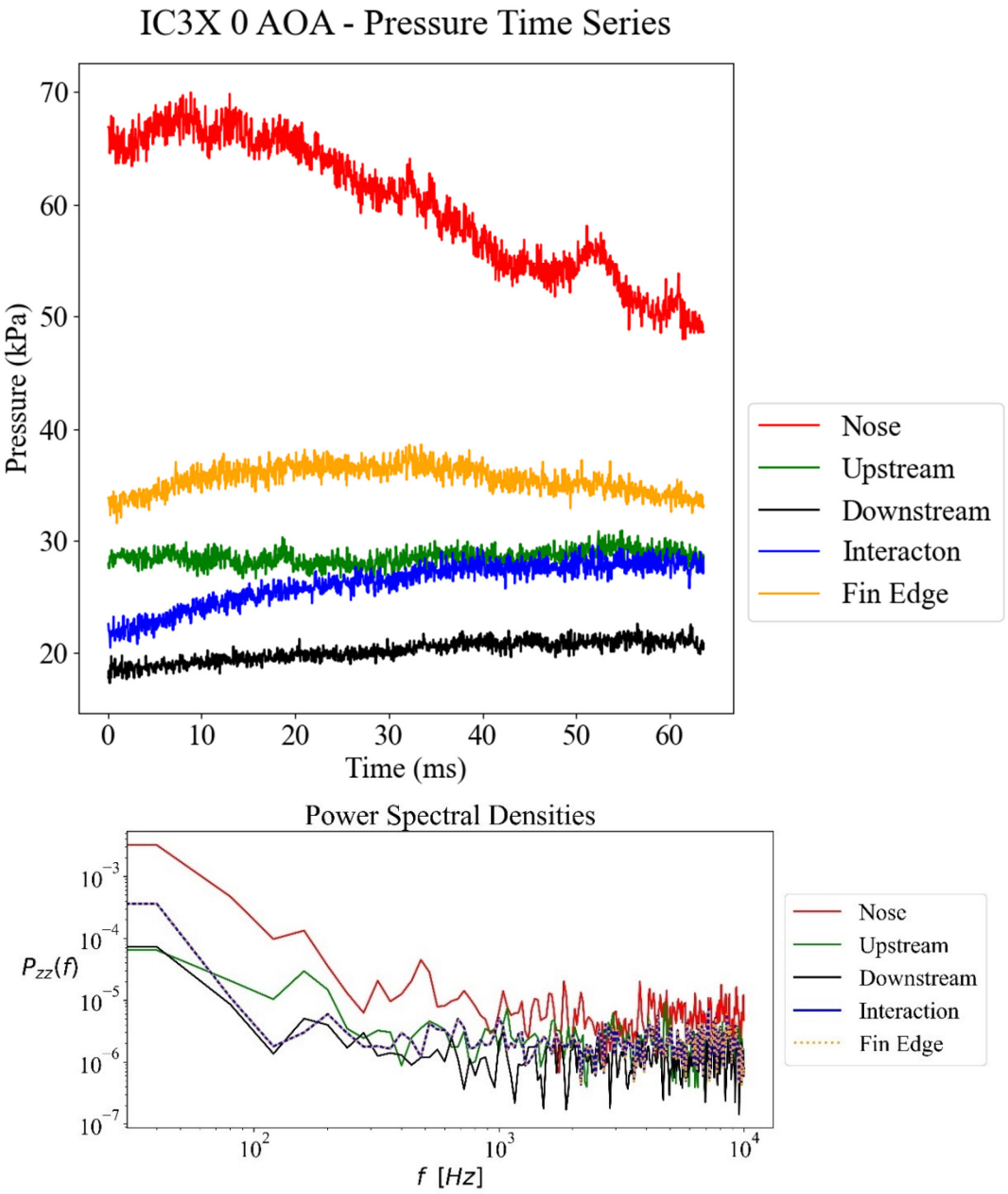

Figure 13. Pressure time histories and power spectral densities at various locations on the vehicle surface at 0° AoA under hypersonic flow.

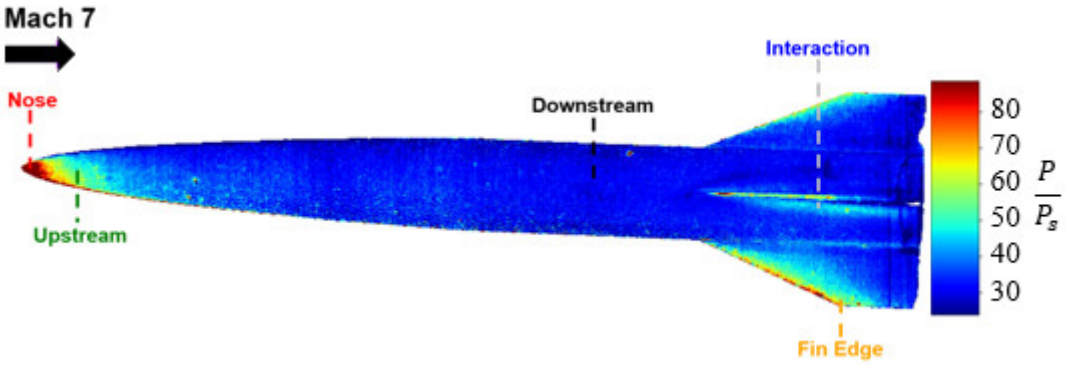

Figure 14. *Cont.*

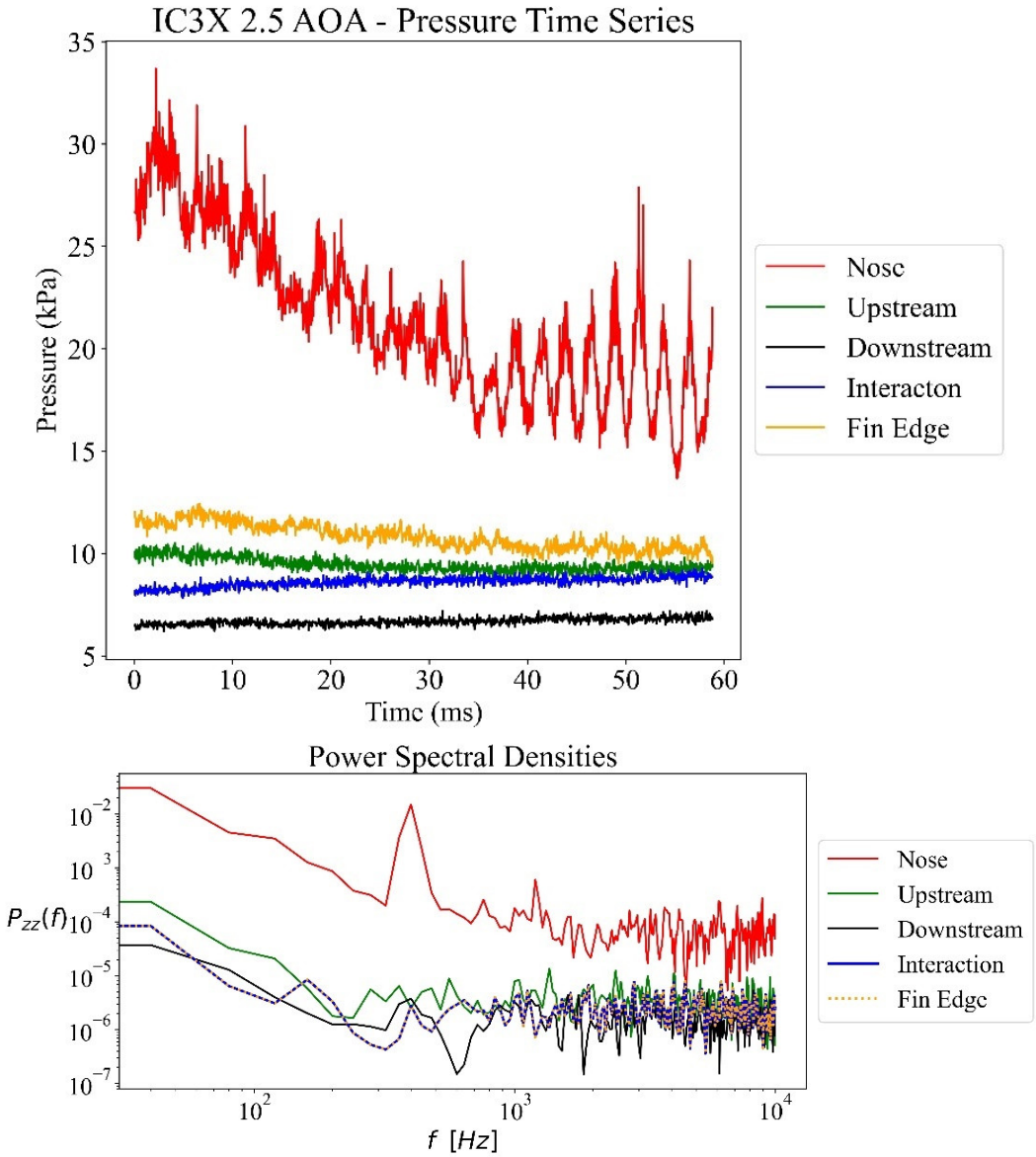

Figure 14. Pressure time histories and power spectral densities at various locations on the vehicle surface at 2.5° AoA under hypersonic flow.

The pressure time histories show that, as expected, the nose of the hypersonic vehicle experiences the highest pressure, with an average of 18 kPa at 0° AoA and 23 kPa at 2.5 AoA. While the pressure at the nose decreases with time, pressures at the upstream, interaction, and fin edge locations remain relatively steady throughout the duration of the steady-state pass. The lowest pressure readings were found downstream of the ogive to the constant cylinder geometry transition for both cases. The pressure oscillations recorded on the nose show a steep decline, suggesting that this is a result of model movement during the test. Upon closer examination of the power spectral density trends, it can be observed that the interaction region and fin edge exhibit similar frequency ranges, with magnitudes that are multiples of each other in the 0° AoA case and corresponding magnitudes in the 2.5° AoA case.

The pressure distribution reveals a significant standard deviation In the nose region, which is expected to be less stable than in the other areas and experience the bending to which this deviation is attributed. Downstream of the model, the pressure stabilizes with a maximum deviation of 7% from the average. Figure 15 illustrates the spread of pressure measurements at the same locations of interest for both cases.

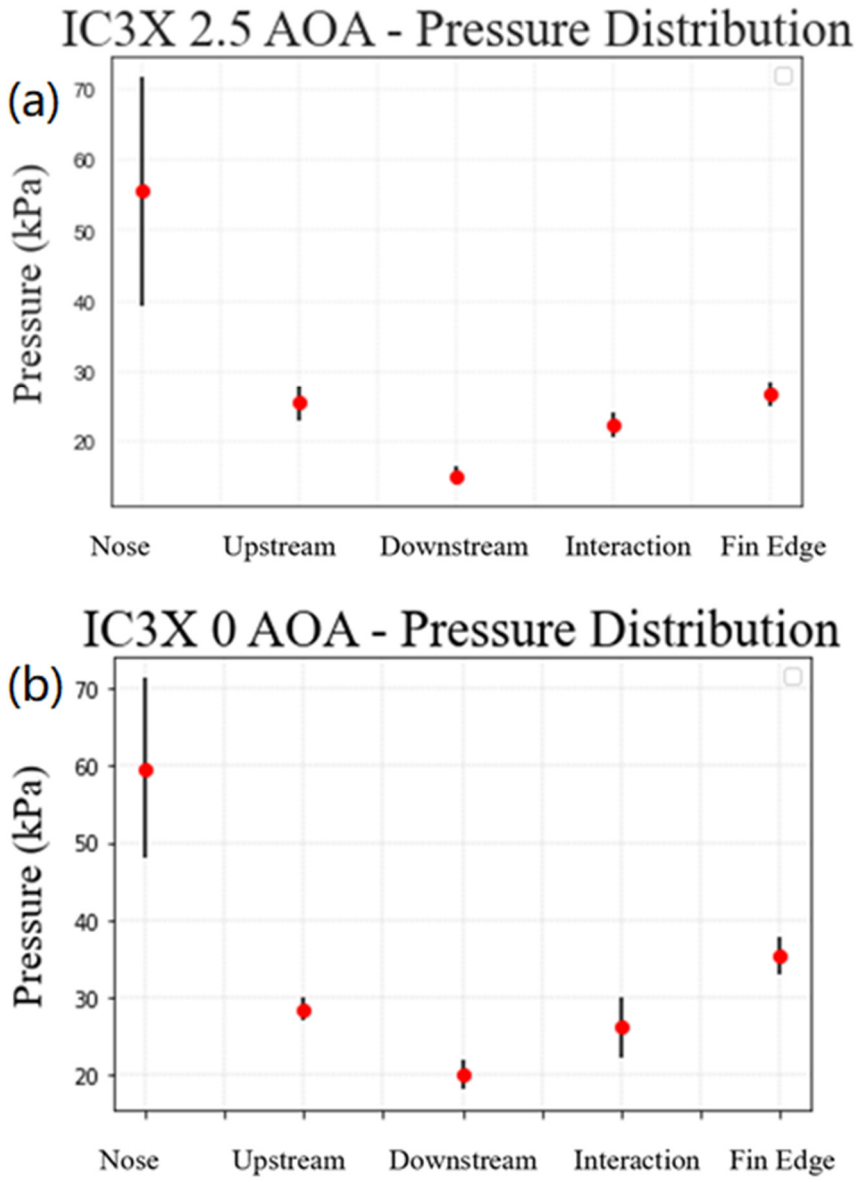

Figure 15. Pressure distribution at various locations on the model surface at (**a**) 2.5° AoA and (**b**) 0° AoA.

The probability density function curves shown below on Figure 16 indicate a wide range of possible pressure values for the nose region in both cases, while the range narrows significantly for the remaining locations.

3.6. POD Analysis

Proper orthogonal decomposition (POD) is a popular technique for identifying key structures in fluid flow. POD was introduced to the fluid dynamics community by Lumley in 1967 [40] and has been used extensively in studies of turbulence. It is used to represent fluid motion as a set of decomposed basis vectors (also called modes) alongside their energy contributions to the overall flow field. Here, we used this technique to identify dominant modes and unsteady structures embedded in the surface pressure data. Accordingly, POD analysis was conducted on the 0° and 2.5° AoA data sets, consisting of 1272 and 1176 snapshots, respectively. The POD modes were computed using MATLAB's Welch power spectral density estimate function. The modes were arranged in decreasing energy, with the first mode containing the highest energy and representing the most dominant flow structure in the data. Sample modes between modes 1-200 for both 0° and 2.5° are provided in Figures 17 and 18 respectively.

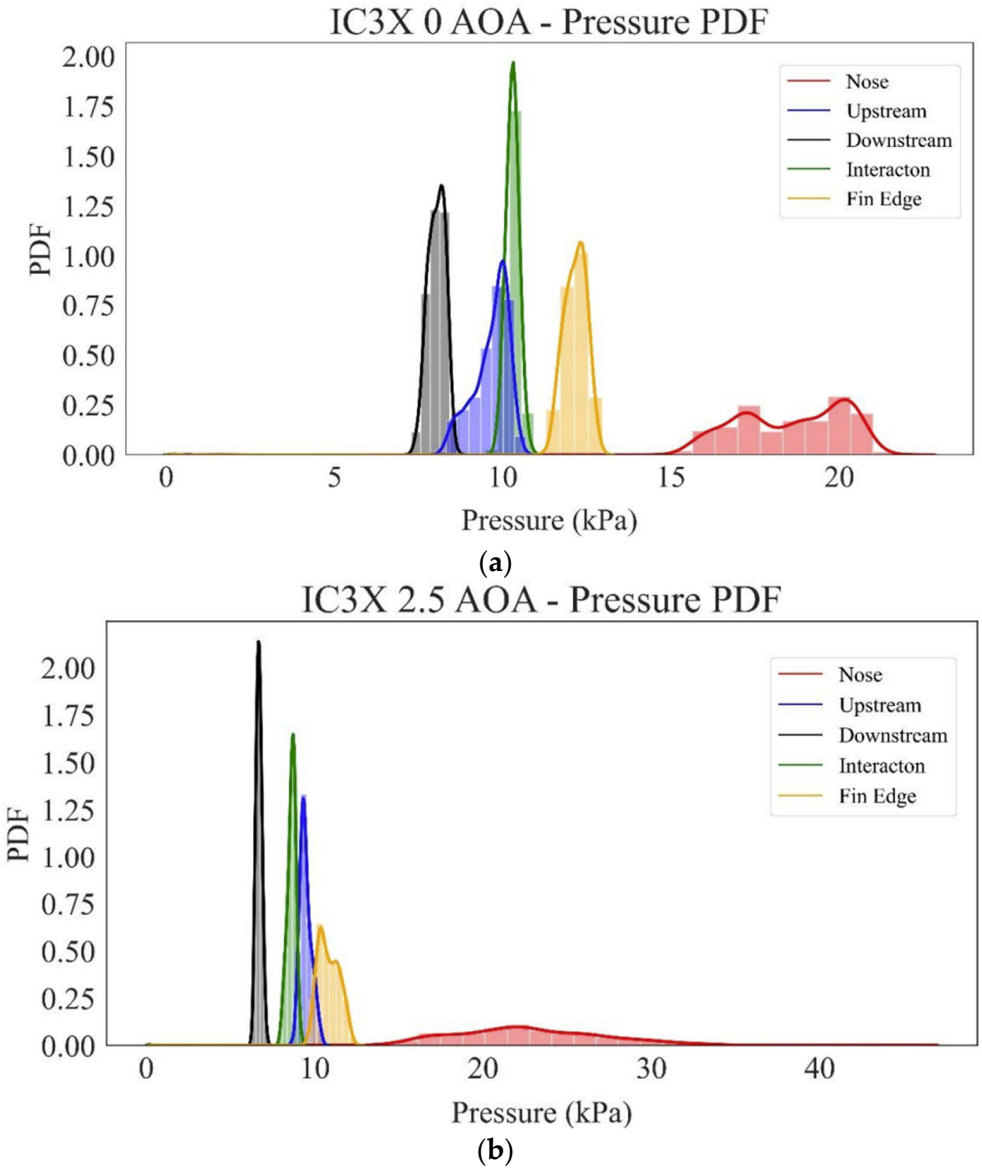

Figure 16. Probability density function curves derived from PSP pressure measurements at various locations of interest at (**a**) 0° AoA and (**b**) 2.5° AoA under hypersonic flow.

The first mode represents the mean surface pressure distribution for both the 0° and 2.5° AoA cases. Similarly, mode 2 of both cases and mode 4 of the 2.5° AoA case highlight areas of compression, such as the nose and fin edges. Mode 3 of the 0° AoA case suggests the existence of a slight lift force acting upon the nose of the model, potentially causing light bending. Mode 2 of the 2.5° AoA case shows a stronger lift force acting on the nose, as expected, at a higher AoA. However, in mode 4 of the 2.5° AoA case, the pressure distribution indicates a downforce or a reaction force from bending.

It should be noted that specific patterns observed in modes 4 and 7 of the 0° AoA case, as well as modes 3, 5, and 6 of the 2.5° AoA case, may initially appear as traveling waves. However, upon closer inspection, these patterns were found to be associated with unevenness in the illumination of the PSP area, which is likely enhanced by the displacement of the wind tunnel during the test. Furthermore, vertical and horizontal striations are noticeable in the instantaneous and average images, which are non-physical and attributed to camera noise. After the fourth mode in both AoA cases, the latter modes continue to highlight these striations, becoming more discernible after mode 8. Figure 19 provides an overview of the energy content for each mode.

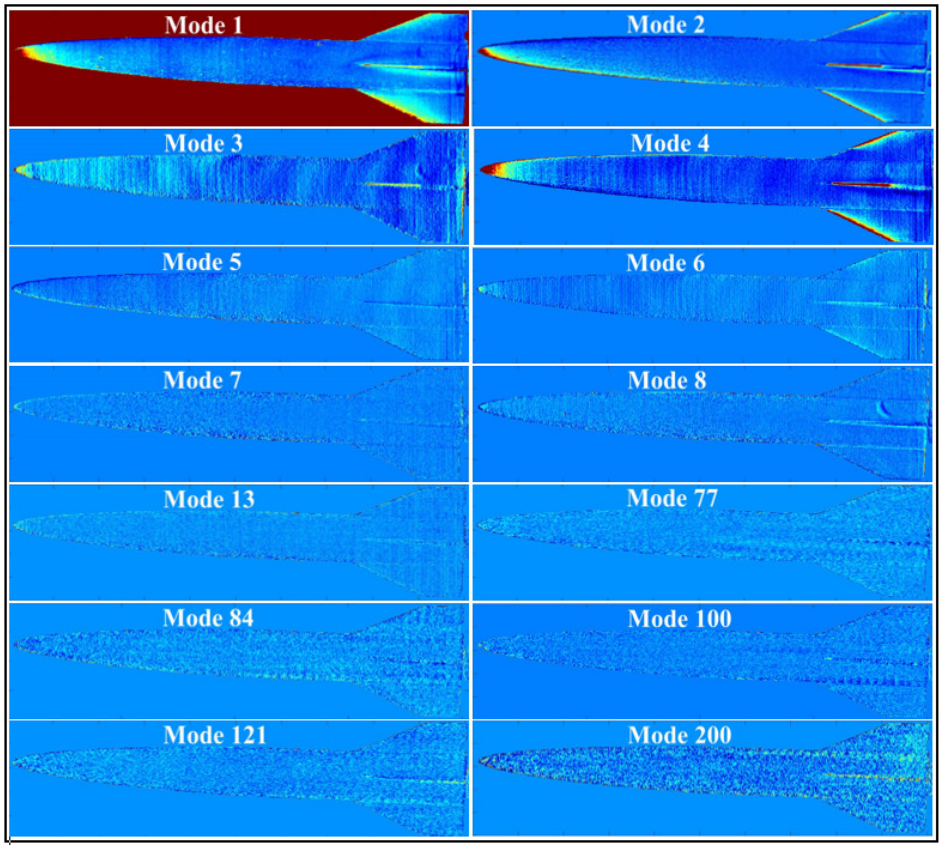

Figure 17. Results of 0° AoA mode 1-200.

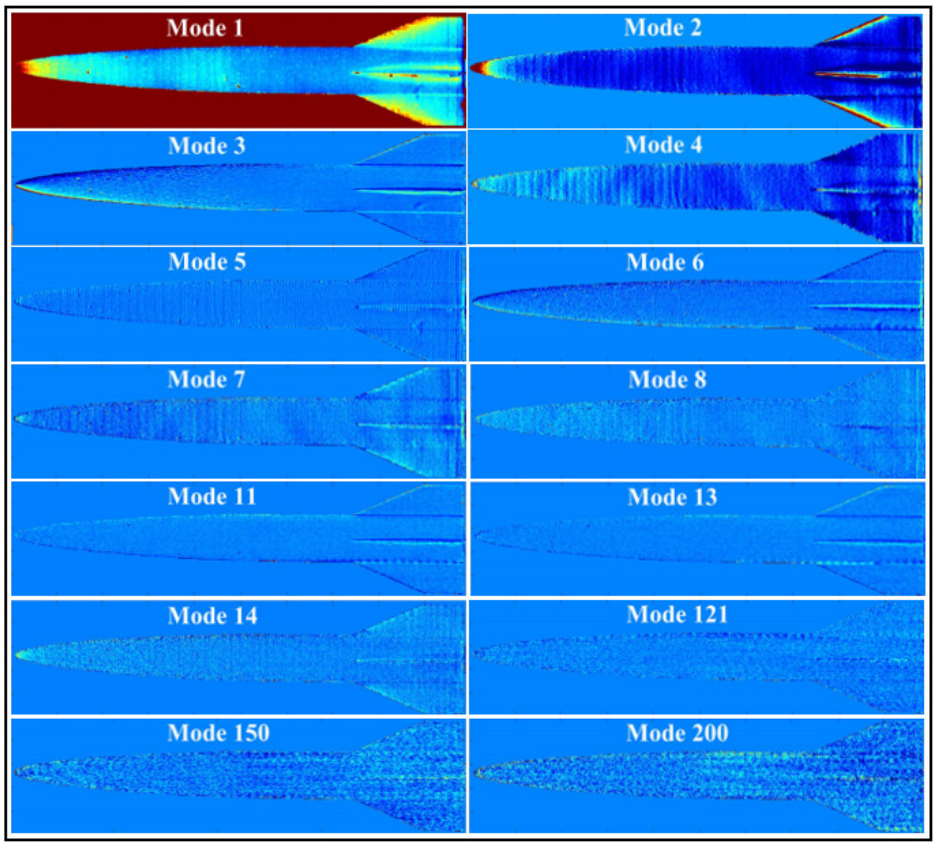

Figure 18. Results of 2.5° AoA Mode 1-200.

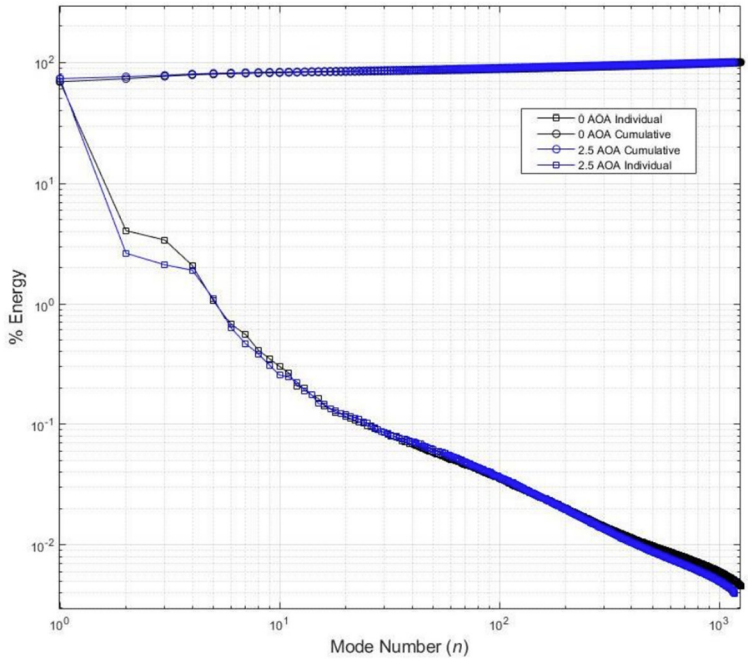

Figure 19. POD mode energy vs. mode number.

3.7. Theoretical Analysis

In addition to the qualitative analysis of pressure distribution using Schlieren imaging, a theoretical analysis was conducted to examine the behavior of supersonic flow over the IC3X model nose. The Taylor–Maccoll relations, which describe the flow properties over a cone, were used to analyze the pressure at the cone surface based on Mach number, cone half angle, and the ratio of specific heats [1]. Since the IC3X model has an ogive shape resembling a nose cone, the Taylor–Maccoll relations were applied to the 0° AoA images for analysis.

Ten pixels, or optical sensors, located on the leading edge were selected for the analysis and are depicted in Figure 20. The pressure time series from these sensors during the first steady-state pass is shown in Figure 21.The sensor averages and standard deviations throughout the steady-state pass are presented in Figure 22, and the probability density functions (PDFs) of the pressure measurements are shown in Figure 23.

The pressure measurements directly at the nose exhibit higher values and greater deviations, averaging at 37 kPa and ranging from 13 to 68 kPa. The PDF indicates that pressure values between 25 and 40 kPa are more likely. The pressure decreases downstream, with an average of 33 kPa for the 2a-2d sensors and 27 kPa for the 3a-3d sensors. As described earlier, the deviations were predominantly due to model movement/bending during the test. The theoretical pressure on the cone surface was calculated using the Virginia Tech Compressible Flow Calculator, considering the freestream Mach number, cone half angle, and ratio of specific heats. The calculated pressure at the cone surface (P_2) varies based on different Mach numbers and cone half angles and is shown below. The average cone angle calculated from the chosen optical sensors is 19.45°. From the pressure time histories depicted in Figure 21, an average pressure for the first steady-state pass was calculated to be 31kPa, which bears a close agreement with the theoretical predictions, as shown in Figure 24.

The trend observed indicates that for a Mach number range of 7.2 ± 0.2, the maximum deviation in pressure is ± 0.5 kPa at lower half-cone angles, increasing to about ± 2 kPa at higher half-cone angles. These calculations predict a static pressure at the cone surface within a 8 to 30 kPa range. The error bars for the experimentally calculated nose pressure and the corresponding half-cone angle are provided. The agreement between the experimental and theoretical pressure measurements for 0° AoA provides confidence in the

presented results. The pressure trends observed on the 2.5° AoA show similar trends, as visualized by Diaz [41] in their CFD work at Mach 5.

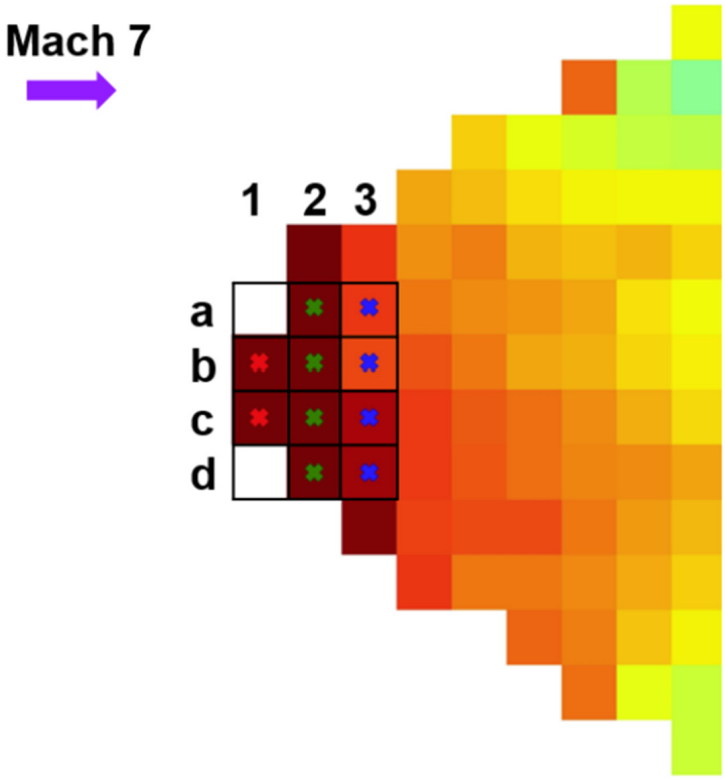

Figure 20. Optical sensors on the IC3X leading edge.

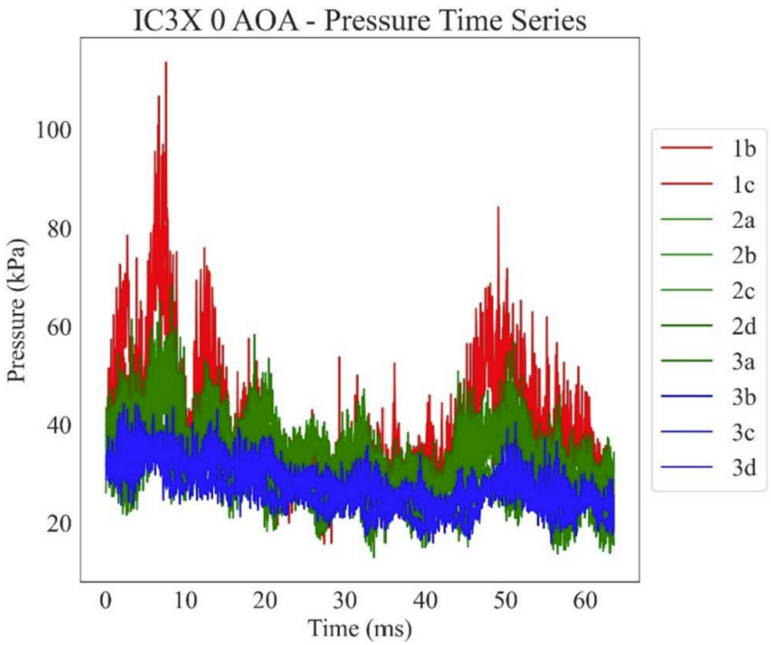

Figure 21. Pressure time series of the IC3X model stagnation location at 0° AoA.

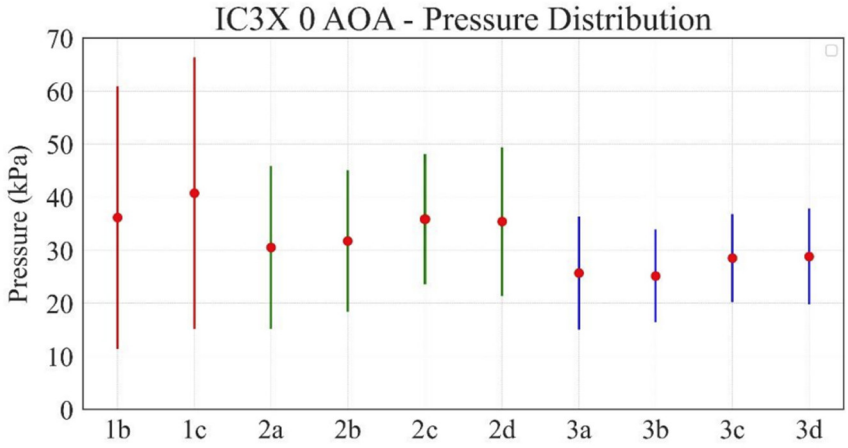

Figure 22. Pressure error bar of the IC3X model stagnation location at 0° AoA.

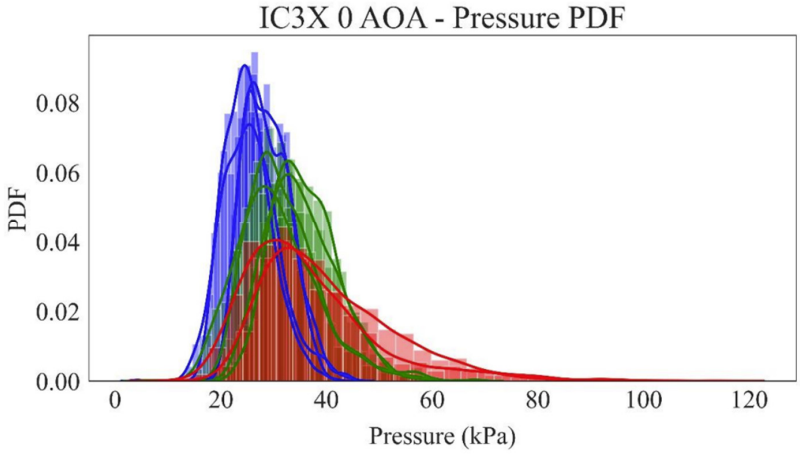

Figure 23. PDF of the IC3X model stagnation pressure at 0° AoA.

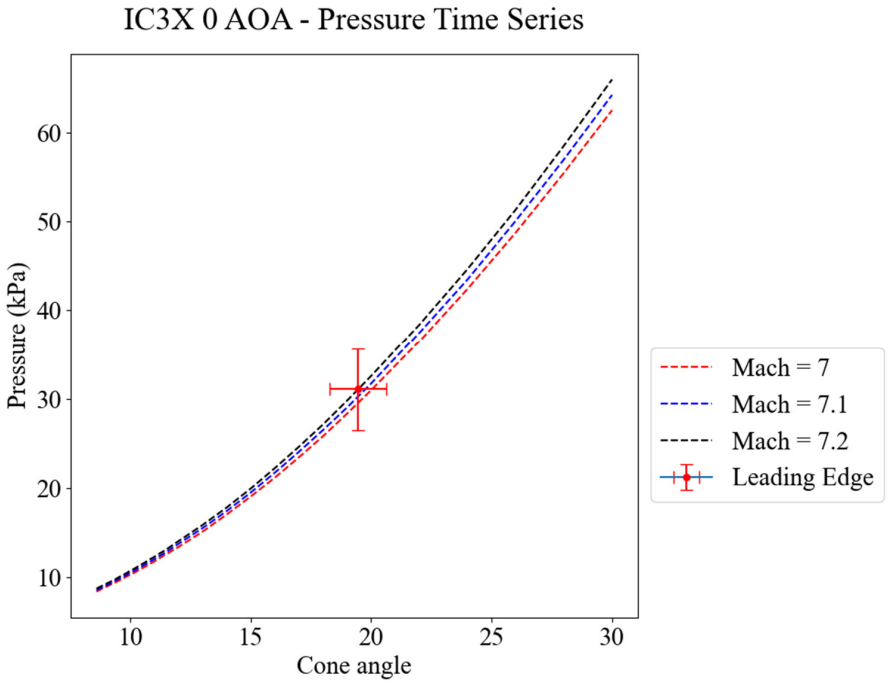

Figure 24. Theoretical pressure on the IC3X model P_2 at M = 7.2 + 0.2, γ = 1.4 over half cone angle θ = 8°–20° at 0° AoA.

4. Conclusions

In conclusion, this study successfully demonstrated the use of pressure-sensitive paint (PSP) to measure surface pressures on a hypersonic concept vehicle under Mach 7 airflow at 0° and 2.5° AoAs. The results were compared with those of Schlieren imaging to identify flow structures and validate the pressure distribution. The analysis of conical shock behavior demonstrated the good agreement between the theoretical and experimental surface pressure ranges at the nose of the model. The preliminary 2D pressure distribution maps derived from PSP measurements aligned with the expected pressure distribution based on the Schlieren images. The observed fluctuations from the average pressure field were primarily located at the model's geometry edges, likely due to model bending that the image registration algorithm cannot entirely correct. The probability density functions (PDFs) and pressure time series highlighted the variation in pressure measurements near the model's edges. The proper orthogonal decomposition (POD) analysis showed that significant energy content was captured within the first few modes, indicating dominant flow patterns. Further investigation is needed to validate the presence of these flow structures using higher-resolution images and accounting for illumination effects during model translation.

The study demonstrated the suitability of pressure-sensitive paint for characterizing surface pressure fields in hypersonic applications. Future experiments will focus on quantifying paint degradation, considering roughness effects, and conducting dynamic calibrations. In addition to this, CFD simulations on the IC3X at multiple angles of attack will also be carried out for secondary validation. These efforts will further enhance the understanding and accuracy of pressure-sensitive paint measurements in the UTSA M7 facility.

Author Contributions: Conceptualization, C.S.C.; methodology, V.D.E. and C.S.C.; software, V.D.E. and A.D.; formal analysis, A.D. and V.D.E.; investigation, A.D. and V.D.E.; data curation, V.D.E.; writing—original draft preparation, V.D.E. and A.D.; writing—review and editing, A.D. and C.S.C.; supervision, C.S.C.; project administration, C.S.C.; funding acquisition, C.S.C. All authors have read and agreed to the published version of the manuscript.

Funding: This work was sponsored (in part) by the Air Force Office of Scientific Research, USAF, under grant/contract number FA9550-21-1-0089. Additional support was provided by NASA grant 80NSSC19M0194. The views and conclusions contained herein are those of the authors and should not be interpreted as necessarily representing the official policies or endorsements, either expressed or implied, of the Air Force Office of Scientific Research, NASA, or the U.S. Government.

Data Availability Statement: Data presented in this study are available on request from the corresponding author.

Acknowledgments: This work was sponsored (in part) by the Air Force Office of Scientific Research, USAF, under grant/contract number FA9550-21-1-0089. Additional support was provided by NASA grant 80NSSC19M0194. The views and conclusions contained herein are those of the authors and should not be interpreted as necessarily representing the official policies or endorsements, either expressed or implied, of the Air Force Office of Scientific Research, NASA, or the U.S. Government. The authors would also like to thank Veronika Granado and Kenneth Perez for assistance with data collection; Eugene Hoffman, Elijah Lalonde, and Sofia Gutierrez for help with initial data processing; and all members of the UTSA hypersonic research laboratory for their efforts in this project.

Conflicts of Interest: The authors declare no conflict of interest. The funders had no role in the design of the study; in the collection, analyses, or interpretation of data; in the writing of the manuscript; or in the decision to publish the results.

Nomenclature

f	Frequency (kHz)
P_{zz}	One-sided power spectral density
I	Intensity (a.u)
I_0	Wind off Intensities (a.u)
I_{ref}	Wind on Intensities (a.u)
AoA	Angle of attack
P_s	Static pressure (kPa)
P_{ref}	Reference pressure (kPa)

References

1. Anderson, J.D. *Modern Compressible Flow with Historical Perspective*; McGraw-Hill: New York, NY, USA, 1982.
2. Johnston, E.W. Current and Advanced X-15. *J. Aircr.* **1965**, *2*, 493–498. [CrossRef]
3. Bertin, J.J.; Cummings, R.M. Fifty Years of Hypersonics: Where We've Been, Where We're Going. *Prog. Aerosp. Sci.* **2003**, *39*, 511–536. [CrossRef]
4. Gardner, A.D.; Klein, C.; Sachs, W.E.; Henne, U.; Mai, H.; Richter, K. Investigation of Three-Dimensional Dynamic Stall on an Airfoil Using Fast-Response Pressure-Sensitive Paint. *Exp. Fluids* **2014**, *55*, 1807. [CrossRef]
5. Okojie, R.S.; Danehy, P.M.; Watkins, A.N.; Mielke, A.F.; Grinstead, J.H. An Overview of NASA Hypersonic Experimental Diagnostic and Instrumentation Technologies for Ground and Flight Testing. In Proceedings of the 16th AIAA/DLR/DGLR International Space Planes and Hypersonic Systems and Technologies Conference, Bremen, Germany, 19–22 October 2009.
6. Chowdhary, K.; Hoang, C.; Lee, K.; Ray, J.; Weirs, V.G.; Carnes, B. Calibrating Hypersonic Turbulence Flow Models with the HIFiRE-1 Experiment Using Data-Driven Machine-Learned Models. *Comput. Methods Appl. Mech. Eng.* **2022**, *401*, 115396. [CrossRef]
7. Powell, J.M.; Murman, S.M.; Ngo, C.L.; Roozeboom, N.H.; Murakami, D.D.; Baerny, J.K.; Li, J. Development of Unsteady-Psp Data Processing and Analysis Tools for the Nasa Ames Unitary 11ft Wind Tunnel. In Proceedings of the AIAA Scitech 2020 Forum, Orlando, FL, USA, 6–10 January 2020.
8. Roozeboom, N.H.; Powell, J.; Baerny, J.K.; Murakami, D.D.; Ngo, C.L.; Garbeff, T.J.; Ross, J.C.; Flach, R. Development of Unsteady Pressure-Sensitive Paint Application on Nasa Space Launch System. In Proceedings of the AIAA Aviation 2019 Forum, Dallas, TX, USA, 17–21 June 2019.
9. Lash, E.L.; Roozeboom, N.H.; Baerny, J.K.; Garbeff, T.J. Preliminary Unsteady Characterization of Shock Wave/Boundary Layer Interactions on a 4% Scale SLS Model Using Upsp and Shadowgraph. In Proceedings of the AIAA AVIATION 2020 FORUM, Virtual. 15–19 June 2020.
10. Li, J.; Lash, E.L.; Roozeboom, N.H.; Garbeff, T.J.; Henze, C.E.; Murakami, D.D.; Smith, N.T.; Baerny, J.K.; Hand, L.A.; Shaw-Lecerf, M.A.; et al. Dynamic Mode Decomposition of Unsteady Pressure-Sensitive Paint Measurements for the NASA Unitary Plan Wind Tunnel Tests. In Proceedings of the AIAA Science and Technology Forum and Exposition, AIAA SciTech Forum 2022, San Diego, CA, USA, 3–7 January 2022.
11. Running, C.L.; Sakaue, H.; Juliano, T.J. Hypersonic Boundary-Layer Separation Detection with Pressure-Sensitive Paint for a Cone at High Angle of Attack. *Exp. Fluids* **2019**, *60*, 23. [CrossRef]
12. Hubner, J.P.; Carroll, B.F.; Schanze, K.S.; Ji, H.F.; Holden, M.S. Temperature- and Pressure-Sensitive Paint Measurements in Short-Duration Hypersonic Flow. *AIAA J.* **2001**, *39*, 654–659. [CrossRef]
13. Wong, O.D.; Neal Watkins, A.; Ingram, J.A.L. Pressure Sensitive Paint Measurements on 15% Scale Rotor Blades in Hover. In Proceedings of the 35th AIAA Fluid Dynamics Conference and Exhibit, Toronto, ON, Canada, 6–9 June 2005.
14. Juliano, T.J.; Kumar, P.; Peng, D.; Gregory, J.W.; Crafton, J.; Fonov, S. Single-Shot, Lifetime-Based Pressure-Sensitive Paint for Rotating Blades. *Meas. Sci. Technol.* **2011**, *22*, 085403. [CrossRef]
15. Gregory, J.W. Porous Pressure-Sensitive Paint for Measurement of Unsteady Pressures in Turbomachinery. In Proceedings of the AIAA Paper, Reno, NV, USA, 5–8 January 2004.
16. Millen, K.M. Characterization of Flow through a Duct Using Pressure-Sensitive Paint, Flow Visualization, and Computational Fluid Dynamics. Ph.D. Thesis, Bradley University, Peoria, IL, USA, 2017.
17. Crites, R.C.; Benne, M.E. Emerging Technology for Pressure Measurement-Pressure Sensitive Paint. In Proceedings of the 33rd Aerospace Sciences Meeting and Exhibit, Reno, NV, USA, 9–12 January 1995.
18. Gregory, J.W.; Asai, K.; Kameda, M.; Liu, T.; Sullivan, J.P. A Review of Pressure-Sensitive Paint for High-Speed and Unsteady Aerodynamics. *Proc. Inst. Mech. Eng. Part G J. Aerosp. Eng.* **2008**, *222*, 249–290. [CrossRef]
19. Ogg, D.R.; Rice, B.E.; Peltier, S.J.; Staines, J.T.; Claucherty, S.L.; Combs, C.S. Simultaneous Stereo Digital Image Correlation and Pressure-Sensitive Paint Measurements of a Compliant Panel in a Mach 2 Wind Tunnel. In Proceedings of the 2018 Fluid Dynamics Conference, Atlanta, GA, USA, 25–29 June 2018.
20. Stern, O.; Volmer, M. Über Die Abklingzeit Der Fluoreszenz. *Physik* **1919**, *20*, 183–188.
21. Liu, T. Pressure- and Temperature-Sensitive Paints. In *Encyclopedia of Aerospace Engineering*; Springer: Berlin/Heidelberg, Germany, 2011.

22. Dale, G.A.; Baust, H.D.; Clinehens, G.A. Implementing Pressure-Sensitive Paint in the AFRL Subsonic Aerodynamic Research Laboratory. In Proceedings of the ICIASF Record, International Congress on Instrumentation in Aerospace Simulation Facilities, Toulouse, France, 14–17 June 1999.
23. McLachlan, B.G.; Bell, J.H. Pressure-Sensitive Paint in Aerodynamic Testing. *Exp. Therm. Fluid Sci.* **1995**, *10*, 470–485. [CrossRef]
24. Chin, D.; Sealy, W.; Granlund, K.; Hayashi, T.; Sakaue, H. Unsteady PSP Measurements on a Cylinder Translating out from a Supersonic Cavity. In Proceedings of the 47th AIAA Fluid Dynamics Conference, Denver, CO, USA, 5–9 June 2017.
25. Numata, D.; Ohtani, K. Surface Pressure Measurement on Supersonic Free-Flight Projectiles Using Unsteady PSP Techniues. In Proceedings of the 2018 Aerodynamic Measurement Technology and Ground Testing Conference, Atlanta, GA, USA, 25–29 June 2018.
26. Running, C.L.; Juliano, T.J. Global Measurements of Hypersonic Shock-Wave/Boundary-Layer Interactions with Pressure-Sensitive Paint. *Exp. Fluids* **2021**, *62*, 1–18. [CrossRef]
27. Nakakita, K.; Asai, K. Pressure-Sensitive Paint Application to a Wing-Body Model in a Hypersonic Shock Tunnel. In Proceedings of the 22nd AIAA Aerodynamic Measurement Technology and Ground Testing Conference, St. Louis, MO, USA, 24–26 June 2002.
28. Hoffman, E.N.A.; Lalonde, E.J.; Garcia, M.; Valeria Delgado, E.; Chen, I.; Bilbo, H.A.; Combs, C.S. Characterization of the UTSA Mach 7 Ludwieg Tube. In Proceedings of the AIAA Science and Technology Forum and Exposition, AIAA SciTech Forum 2022, San Diego, CA, USA, 3–7 January 2022.
29. Hoffman, E.N.A.; Lalonde, E.J.; Andrade, A.; Chen, I.; Bilbo, H.A.; Combs, C.S. Flow Characterization of the UTSA Hypersonic Ludwieg Tube. *Aerospace* **2023**, *10*, 463. [CrossRef]
30. Bashor, I.P.; Hoffman, E.; Gonzalez, G.; Combs, C.S. Design and Preliminary Calibration of the Utsa Mach 7 Hypersonic Ludwieg Tube. In Proceedings of the AIAA Aviation 2019 Forum, Dallas, TX, USA, 17–21 June 2019.
31. Hoffman, E.N.A.; Valeria, D.E.; Garcia, M.; Lalonde, E.J.; Rodriguez, J.M.; Combs, C.S. Preliminary Testing of the UTSA Mach 7 Ludwieg Tube. In Proceedings of the AIAA Aviation and Aeronautics Forum and Exposition, AIAA AVIATION Forum 2021, Virtual. 2–6 August 2021.
32. Klock, R.J. Efficient Numerical Simulation of Aerothermoelastic Hypersonic Vehicles. Ph.D. Thesis, University of Michigan, Ann Arbor, MI, USA, 2017.
33. FormLabs Standard Materials for High-Resolution Rapid Prototyping. 2017, pp. 1–3. Available online: https://formlabs-media.formlabs.com/filer_public/ac/89/ac8963db-f54a-4cac-8fe9-fb740a7b06f1/formlabs-materials-library.pdf (accessed on 23 September 2023).
34. Egami, Y.; Hasegawa, Y.; Matsuda, Y.; Ikami, T.; Nagai, H. Ruthenium-Based Fast-Responding Pressure-Sensitive Paint for Measuring Small Pressure Fluctuation in Low-Speed Flow Field. *Meas. Sci. Technol.* **2020**, *32*, 024003. [CrossRef]
35. Smith, C.D.; Kreth, P.A.; Schmisseur, J.D.; Strickland, G. Characterization of Temperature Sensitive Paint for Application in Hypersonic Ludwieg Tubes at the University of Tennessee. In Proceedings of the AIAA Science and Technology Forum and Exposition, AIAA SciTech Forum 2022, San Diego, CA, USA, 3–7 January 2022.
36. Guizar-Sicairos, M.; Thurman, S.T.; Fienup, J.R. Efficient Subpixel Image Registration Algorithms. *Opt. Lett.* **2008**, *33*, 156–158. [CrossRef] [PubMed]
37. OpenCV. Open CV Modules. Available online: https://docs.opencv.org/3.4/index.html (accessed on 23 September 2023).
38. Javh, J.; Slavič, J.; Boltežar, M. The Subpixel Resolution of Optical-Flow-Based Modal Analysis. *Mech. Syst. Signal Process.* **2017**, *88*, 89–99. [CrossRef]
39. Andrade, A.; LaLonde, E.J.; Hoffman, E.N.A.; Tangarife, S.G.; Combs, C.S. Application of Pressure-Sensitive Paint to Investigate Hypersonic Shock-Wave/Boundary-Layer Interactions. In Proceedings of the AIAA SCITECH 2023 Forum 2022, National Harbor, MD, USA, 23–27 January 2022.
40. Lumley, J.L. The Structure of Inhomogeneous Turbulent Flows. In *Proceedings of the International Colloquium on the Fine Scale Structure of the Atmosphere and Its Influence on Radio Wave Propagation*; Nauka: Moscow, Russia, 1967; pp. 166–178.
41. Diaz Villa, B.E. Fluid-Structure Interaction of a Planar Shock Impinging on a One Degree-of-Freedom Axisymmetric Body in Mach 5 Flow. In Proceedings of the 76th Annual Meeting of the Division of Fluid Dynamics, Washington, DC, USA, 19–21 November 2023.